Au Nanorod Design as Light-Absorber in the First and Second Biological Near-Infrared Windows for *in Vivo* Photothermal Therapy

Ming-Fong Tsai,[†] Shih-Hui Gilbert Chang,[‡] Fong-Yu Cheng,[§] Vijayakumar Shanmugam,[†] Yu-Sheng Cheng,[†] Chia-Hao Su,[⊥] and Chen-Sheng Yeh[†,*]

[†]Department of Chemistry, Center for Micro/Nano Science and Technology, and Advanced Optoelectronic Technology Center, [‡]Department of Photonics, and [§]Institute of Oral Medicine, National Cheng Kung University, Tainan, 701 Taiwan and [⊥]Center for Translational Research in Biomedical Sciences, Kaohsiung Chang Gung Memorial Hospital, Kaohsiung, 833 Taiwan

ABSTRACT Photothermal cancer therapy using near-infrared (NIR) laser radiation is an emerging treatment. In the NIR region, two biological transparency windows are located in 650−950 nm (first NIR window) and 1000−1350 nm (second NIR window) with optimal tissue transmission obtained from low scattering and energy absorption, thus providing maximum radiation penetration through tissue and minimizing autofluorescence. To date, intensive effort has resulted in the generation of various methods that can be used to shift the absorbance of nanomaterials to the 650−950 nm NIR regions for studying photoinduced therapy. However, NIR light absorbers smaller than 100 nm in the second NIR region have been scant. We report that a Au nanorod (NR) can be designed with a rod-in-shell (rattle-like) structure smaller than 100 nm that is tailored to be responsive to the first and second NIR windows, in which we can perform hyperthermia-based therapy. *In vitro* performance clearly displays high efficacy in the NIR photothermal destruction of cancer cells, showing large cell-damaged area beyond the laser-irradiated area. This marked phenomenon has made the rod-in-shell structure a promising hyperthermia agent for the *in vivo* photothermal ablation of solid tumors when activated using a continuous-wave 808 m (first NIR window) or a 1064 nm (second NIR window) diode laser. We tailored the UV−vis−NIR spectrum of the rod-in-shell structure by changing the gap distance between the Au NR core and the AuAg nanoshell, to evaluate the therapeutic effect of using a 1064 nm diode laser. Regarding the first NIR window with the use of an 808 nm diode laser, rod-in-shell particles exhibit a more effective anticancer efficacy in the laser ablation of solid tumors compared to Au NRs.

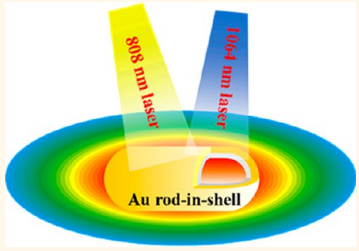

KEYWORDS: photothermal therapy · hyperthermia · Au nanorod · cancer · biological window

Light is an external stimulus and provides considerable benefits in efficacy for a desired time and area in cancer treatment. Photothermal cancer therapy using near-infrared (NIR) laser radiation is an emerging field. This technique provides a minimally invasive alternative to the conventional surgical treatment of solid tumors. Thermal therapeutics is relatively simple to perform and has the advantages of a fast recovery, fewer complications, and shorter hospital stays. Biomedical applications in which both blood and soft tissues are highly penetrable require a considerably deeper penetration of NIR light. The laser wavelength used in photothermal treatment is highly desired in the NIR region. In the NIR region, two biological transparency windows are located in 650−950 nm (first NIR window) and 1000−1350 nm (second NIR window), with optimal tissue transmission obtained from low scattering and energy absorption, thus providing maximum radiation penetration through tissue and minimizing autofluorescence.[1−3] The second region between 1000 and 1350 nm is recognized to offer more efficient tissue penetration relative to the first region of 650−950 nm when considering absorption and scattering effects in tissue. For example, hemoglobin has substantially less absorption in the NIR wavelength, and blood is sufficiently transparent from 1000 to 1350 nm. Materials absorbing radiation in the NIR range are considered suitable agents for photothermal cancer therapy.

* Address correspondence to csyeh@mail.ncku.edu.tw.

Received for review March 8, 2013 and accepted May 7, 2013.

Published online May 07, 2013
10.1021/nn401187c

To date, intensive efforts in photoinduced therapy have resulted in various methods on the shifting absorbance of nanomaterials to the 650−950 nm NIR regions.[4−14] In contrast, nanomaterials responsive in the second NIR region are limited. The PbS,[15] PbSe,[15,16] and Ag_2S quantum dots[3] and single-wall carbon nanotubes[2] have the characteristics of NIR fluorophores with an emission wavelength of 1000 to 1400 nm. An NIR light absorber smaller than 100 nm in the second NIR region is substantially limited compared to NIR fluorophores.[17,18] Considering the importance of the NIR stimulus in biomedical applications, the construction of nanoabsorbers, which are responsive to the wavelength of the second NIR region, is still an incipient area and in strong demand. A Au nanorod (NR) is a classic nanomaterial that is recognized to effectively exhibit the promising NIR hyperthermia effect.[19−27] The longitudinal absorbance of a Au NR is sensitive to the aspect ratio (length/width) and can be easily tuned to 800 nm, as well as maintain a size below 100 nm. Preparing a Au NR (<100 nm) with a surface plasmon resonance (SPR) band extended to 1000 nm remains challenging. The length of a Au NR is usually prolonged to 300−600 nm if its longitudinal modes appear in the second NIR region.[28−31] By carefully selecting a Au seed, Mulvaney and co-workers prepared the shortest Au NR, which is 140 nm long, with an SPR peak at 1006 nm.[19] Hamad-Schifferli and co-workers synthesized nanobones (17 nm × 89 nm) with a longitudinal mode of SPR bands that appeared at 1100 nm.[32]

Herein, we report that a Au NR can be designed with a rod-in-shell (rattle-like) structure smaller than 100 nm that is tailored to be responsive to the first and second NIR windows. The developed structure can selectively provide hyperthermia therapy in the first or second NIR window. The rod-in-shell structure shows the approximate range of the broad absorbance band, which is 300−1350 nm with two distinct NIR SPR bands beyond 1000 nm that appear at approximately 1100 and 1280 nm. This rattle-like structure with an approximate length of 53 nm and an approximate width of 26 nm has a Au NR approximately 40 nm long and approximately 10 nm wide, which is encapsulated in a cavity of a AuAg nanoshell. Rod-in-shell particles show a highly efficacious *in vitro* photothermal killing of cancer cells with a destructive area bigger than the illuminated laser spot. This phenomenon has made the rod-in-shell structure a promising hyperthermia agent for the *in vivo* photothermal ablation of solid tumors when triggered using the continuous-wave (CW) 808 nm (first NIR window) or 1064 nm (second NIR window) diode laser. We found that the UV−vis−NIR spectrum of the rod-in-shell structure is sensitive to the gap distance between the Au NR core and the Au/Ag nanoshell. In this context, we tailored the UV−vis−NIR spectrum of the rod-in-shell structure by changing the gap distance between the Au NR core and the Au/Ag nanoshell to evaluate the therapeutic effect by using a 1064 nm diode laser. To the best of our knowledge, this study is the first to show *in vitro* and *in vivo* photothermal cancer therapy in the second NIR window. Regarding the first NIR window with the use of an 808 nm diode laser, rod-in-shell particles exhibit more effective anticancer efficacy in the laser ablation of solid tumors compared to Au NRs.

RESULTS AND DISCUSSION

Synthesis and Characterization of Rod-in-Shells. The Au NRs with an approximate aspect ratio of 4 (approximate length: 40 nm, approximately width: 10 nm) were synthesized using the seedless method (Figure 1a).[33] Following centrifugation and wash processes, Au NRs were collected and redispersed in H_2O, and then subjected to the formation of a Ag nanolayer on their surface by reducing $AgNO_3$ with a mixture of ascorbic acid (AA), cetyltrimethylammonium bromide (CTAB), and polyvinylpyrrolidone (PVP) to yield Au NR@Ag.[34] The transmission electron microscopy (TEM) image in Figure 1b clearly shows a differential contrast with darkened Au NRs embedded in the lighter Ag nanolayer. The thickness of the Ag nanolayer could be varied relative to the change in the $AgNO_3$ amount, and 7−8 nm of the Ag nanoshell was presented as a typical example. The Au NR@Ag products were collected after centrifugation and a wash procedure for rod-in-shell formation. The Au NR@Ag was converted to a Au rod-in-shell structure with a Au/Ag nanoshell in a reaction mixture containing $HAuCl_4$ (700 μL), CTAB, and AA. Adding $HAuCl_4$ triggers Ag nanoshell etching through galvanic corrosion. After a short reaction of 16 min, the rod-in-shell formed with a Au NR embedded in a hollow Au/Ag shell with a distinct gap (Figure 1c). A typical rod-in-shell structure has a length of approximately 53 nm and a width of approximately 26 nm with a 4−5 nm thickness of the Au/Ag nanoshell. We estimate the gap between the Au NR and the Au/Ag nanoshell to be 2 nm, based on the TEM images (Figure 2). We performed energy-dispersive X-ray analysis (EDX) of a single rod-in-shell, which showed the average atomic ratio of Au/Ag to be 47.5/52.5 in the shell (Figure 2b). The elemental maps shown in Figure 2c provide additional evidence for the distribution of Au and Ag elements in the shell. The presence of the Au NR caused condensed Au signal positions in the core. We observed the evolution of the UV−vis−NIR absorption behavior in the course of preparation. Initially, Au NRs display transverse and longitudinal absorbance maxima at 521 and 800 nm, respectively (Figure 1a). Once the Au NR was epitaxially coated with 7−8 nm of a Ag shell, the transverse and longitudinal maxima blue-shifted to 393 and 606 nm (Figure 1b), respectively, because of the different dielectric functions of Ag and Au.[34,35] In addition, a

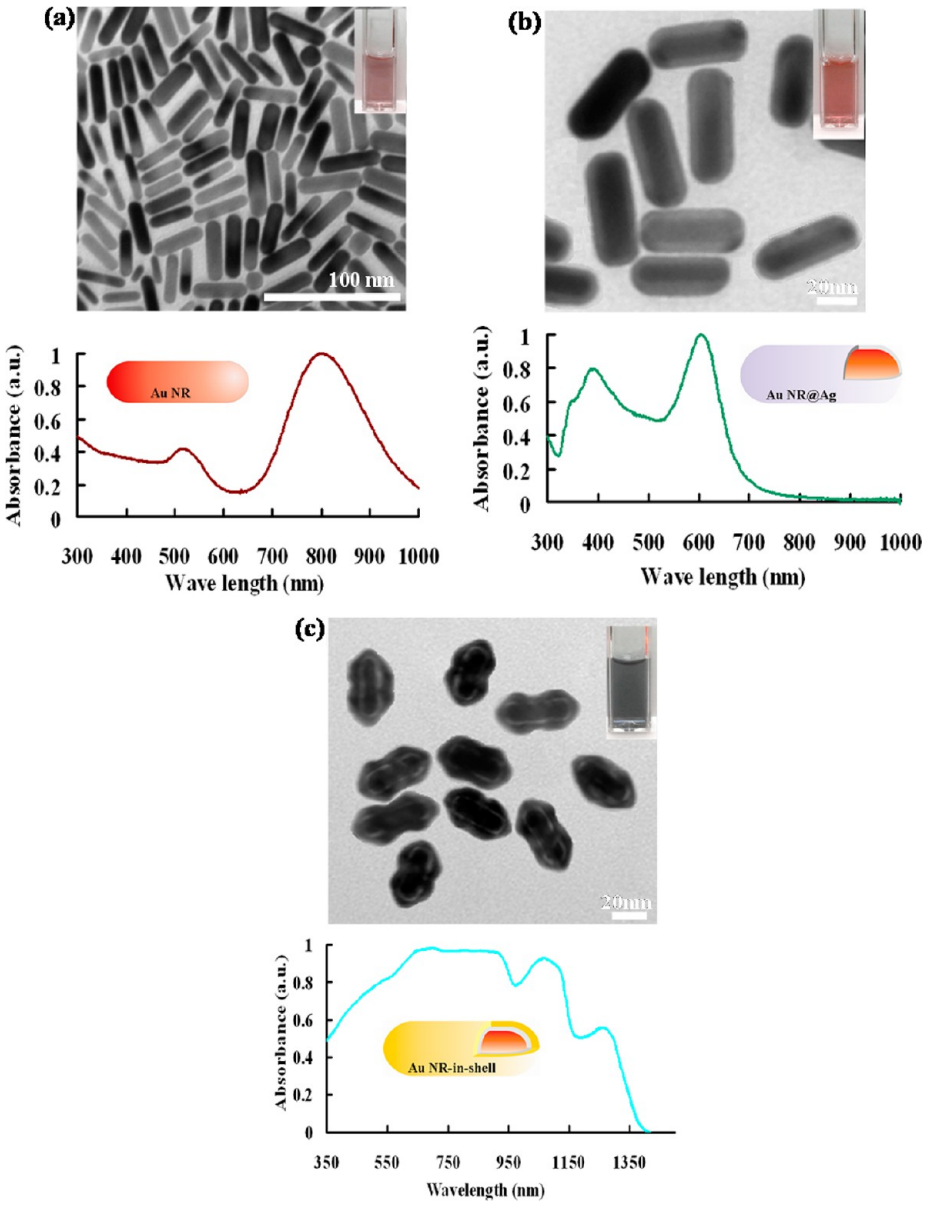

Figure 1. The TEM images, colloidal aqueous solutions (inset), and UV–vis–NIR spectra of resulting (a) Au NRs, (b) Au NR@Ag, and (c) Au rod-in-shell (gap, 2 nm).

small shoulder appeared at 360 nm, which could be attributed to the anisotropic growth mode,[36] indicating that the Ag nanoshell was unevenly deposited on the Au NRs. This thin Ag shell, replaced with Au after the addition of $HAuCl_4$, grew into a rough, dented Au/Ag shell around the core rod, with a distinct dielectric gap between them. We have performed a gas adsorption–desorption method to determine the porosity of rod-in-shell particles. The specific surface area was found to be 24.8 m^2/g using a Brunauer–Emmett–Teller (BET) plot, and the Barret-Joyner-Halenda (BJH) result shows an inhomogeneous pore size distributed in the range of 3–6 nm (Supporting Information, Figure S1). Because of porosity of rod-in-shells, it is thought that the gap between Au NR and shell can be filled with liquid such as water used in our preparation.

The optical behavior of the rod-in-shell exhibits wide absorbance from UV to NIR up to 1350 nm wavelength. Two distinct bands stand at 1100 and 1280 nm. The colloidal solutions changed from reddish (Au NRs) to grayish blue (rod-in-shell). For the measurements shown in Figure 1, the as-prepared Au NRs, Au NR@Ag, and rod-in-shell all underwent H_2O washing and centrifugation, and were then redispersed in H_2O. The rod-in-shell nanoparticles retain their morphology and structure up to 3 months of storage.

The absorbance bands appearing at NIR prompted us to tune the gap between the Au NR and the Au/Ag nanoshell. We added AA so that it could react with the Au NR@Ag in addition to $HAuCl_4$ (for the galvanic reaction), to yield rod-in-shell structures in our preparation, that is, to simultaneously enable the reduction

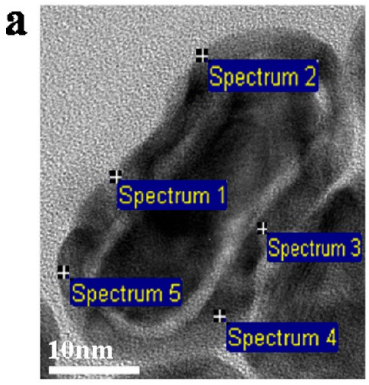

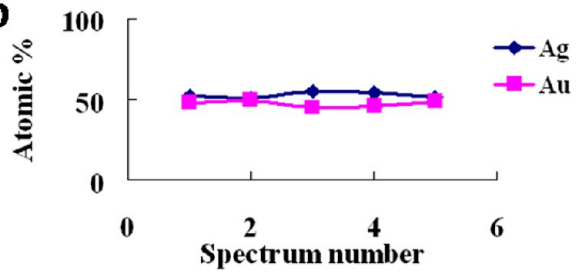

	Spectrum1	Spectrum2	Spectrum3	Spectrum4	Spectrum5
Element	Atomic%	Atomic%	Atomic%	Atomic%	Atomic%
Ag	51.6	50.7	54.9	53.8	51.4
Au	48.4	49.3	45.1	46.2	48.6
Overall	100.0	100.0	100.0	100.0	100.0
Average	**Ag: Au = 52.5: 47.5**				

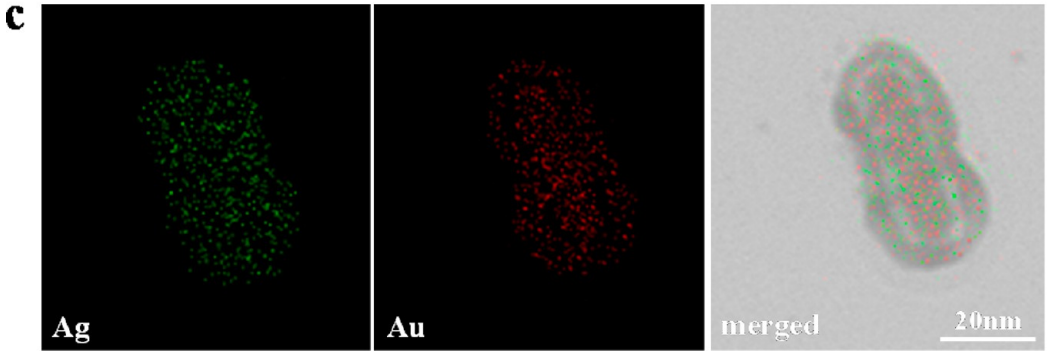

Figure 2. (a) The HRTEM image and (b,c) EDX analysis of rod-in-shell nanoparticles. The spectra 1−5 represent different sites analyzed in the Ag/Au nanoshell. Elemental maps of Ag (green), Au (red), and merged image. The rod-in-shells were prepared by adding 700 μL of $HAuCl_4$ into Au NR@Ag (7−8 nm of Ag nanoshell) colloidal solution containing CTAB and AA.

of Au from AA and the oxidative etching of Ag from $HAuCl_4$ from the reaction solution. With the simultaneous performance of these two reactions, we observed the backfilling phenomenon of the gap, showing an increase in the Au composition deposition, instead of a nanoshell collapse with the addition of excess $HAuCl_4$ through oxidative etching in the galvanic replacement reaction. For example, the Au NR@Ag with a 7- to 8-nm-thick Ag shell in reactions with V_{HAuCl_4} = 550 or 700 μL, respectively, yields a 4 or 2 nm gap (Figures 2 and 3). With an increase in additional $HAuCl_4$, the gap distance decreases with an increase in the atomic ratio of Au/Ag, from 38.9/61.1 (4 nm gap) to 47.5/52.5 (2 nm gap) (Figures 2 and 4). For pure oxidative etching of the replacement reaction, we expected to observe a widened gap with an increase in $HAuCl_4$, instead of a decrease of the gap. To support the occurrence of backfilling, two more reactions were conducted at reduced amounts of V_{HAuCl_4} = 280 and 420 μL from 550 μL, showing an increasing trend in the gap distance, with V_{HAuCl_4} increasing because of the galvanic replacement reaction (Supporting Information, Figure S2). Overall, we are able to tune the gap distance by varying the additional $HAuCl_4$ amount and/or the thickness of the Au NR@Ag in the Ag nanoshell. For the 6.5 nm gap, we used a thicker 9−10 nm shell of the Au NR@Ag to react with V_{HAuCl_4} = 400 μL. Both the 2 and 6.5 nm gaps in the structures have a close dimension. Please refer to the experimental section. Figure 5 shows the obvious change in the gap-tailoring UV−vis−NIR behavior. A gap increase results in a decreased appearance (intensity) of two absorptions at 1100 and 1280 nm. We suggested that the coupling of the central Au NR and the Au/Ag nanoshell strongly affects these two NIR bands.

Theoretical Simulation on the UV−vis−NIR Behavior of Rod-in-Shells. Nordlander and co-workers developed a hybridization model to interpret plasmon modes for dielectric-core-metal-shell nanoparticles.[37] Accordingly, the shell was found to show two plasmons—one symmetrical (bonding, ω_-), and the other asymmetric (antibonding ω_+), generating low- and high-energy absorption, respectively. When another solid metal core is introduced inside the shell cavity,[38] these symmetric and asymmetric modes are expected to interact with the core. (In our case, the core is a rod.) In the same report for a spherical concentric shell−core nanoparticle, the gap is large, and the hybridization

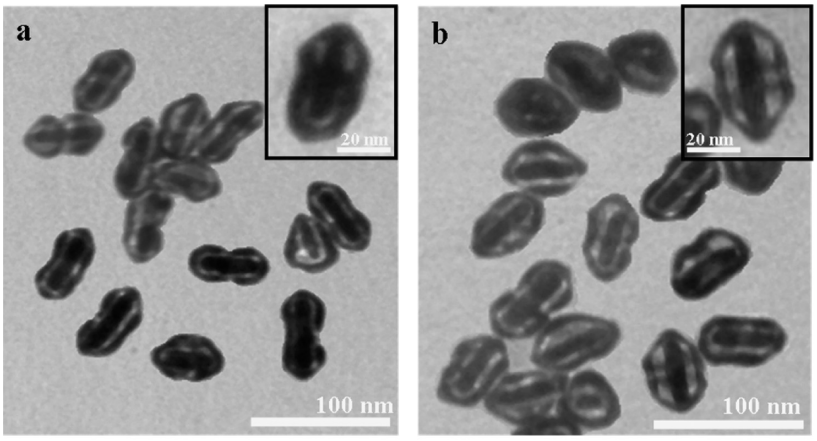

Length : ~54.3 nm
Width : ~28.1nm
Gap: ~4 nm
Shell: ~3.9 nm

Length : ~53.0 nm
Width : ~30.4 nm
Gap: ~6.5 nm
Shell: ~4.0 nm

Figure 3. TEM images of rod-in-shell nanoparticles with (a) gap 4.0 nm, (b) 6.5 nm. Gaps 4.0 and 6.5 nm were respectively prepared by adding 550 μL of $HAuCl_4$ into Au NR@Ag (7−8 nm of Ag nanoshell) and 400 μL of $HAuCl_4$ into Au NR@Ag (9−10 nm of Ag nanoshell) colloidal solutions containing CTAB and AA. The insets show the enlarged single rod-in-shell particles.

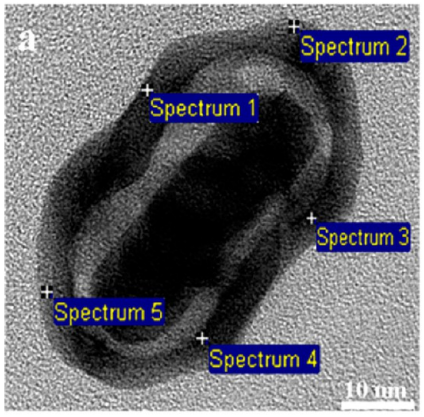

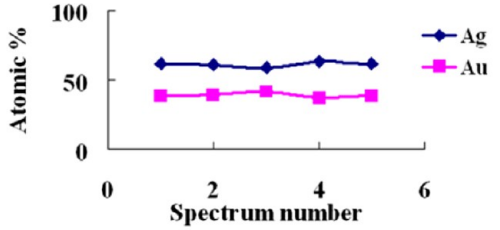

	Spectrum1	Spectrum2	Spectrum3	Spectrum4	Spectrum5
Element	Atomic%	Atomic%	Atomic%	Atomic%	Atomic%
Ag	61.4	60.8	58.7	63.2	61.6
Au	38.6	39.2	41.3	36.8	38.4
Overall	100.0	100.0	100.0	100.0	100.0
Average	**Ag: Au = 61.1: 38.9**				

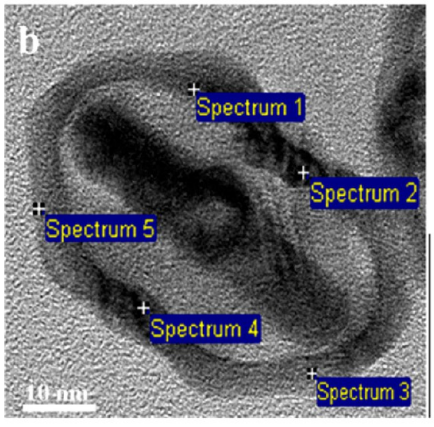

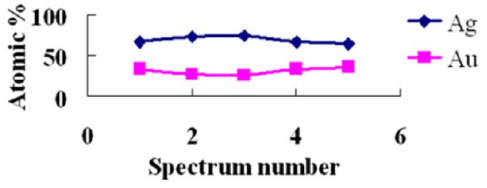

	Spectrum1	Spectrum2	Spectrum3	Spectrum4	Spectrum5
Element	Atomic%	Atomic%	Atomic%	Atomic%	Atomic%
Ag	66.2	72.7	74.2	66.2	64.5
Au	37.1	24.2	25.8	33.8	35.5
Overall	100.0	100.0	100.0	100.0	100.0
Average	**Ag: Au = 68.8: 31.2**				

Figure 4. HRTEM images and EDX analysis of rod-in-shells with (a) gap 4.0 nm (b) 6.5 nm. The spectrum 1−5 shown in each rod-in-shell represents different spot site analyzed in the Ag/Au shell. Gaps 4.0 and 6.5 nm were respectively prepared by adding 550 μL of $HAuCl_4$ into Au NR@Ag (7−8 nm of Ag nanoshell) and 400 μL of $HAuCl_4$ into Au NR@Ag (9−10 nm of Ag nanoshell) colloidal solutions containing CTAB and AA.

model has only three modes.[38] In our rod-in-shell structure with cylindrical symmetry, further surface plasmon (SP) mode splitting is possible because of the small gap. In this rattle-like structure, the cavity

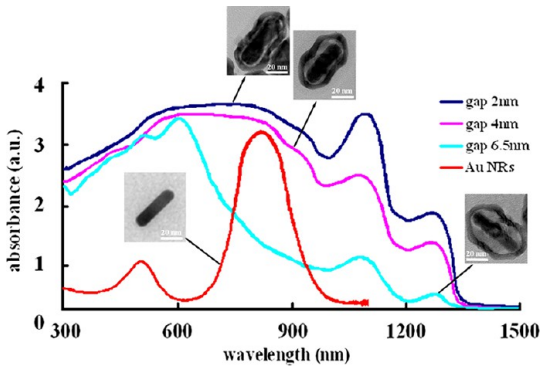

Figure 5. The UV–vis–NIR spectra of Au rod-in-shells with different gaps and Au nanorods, measured at the same dosage amount of 50 ppm (in Au concentration), and their corresponding TEM images.

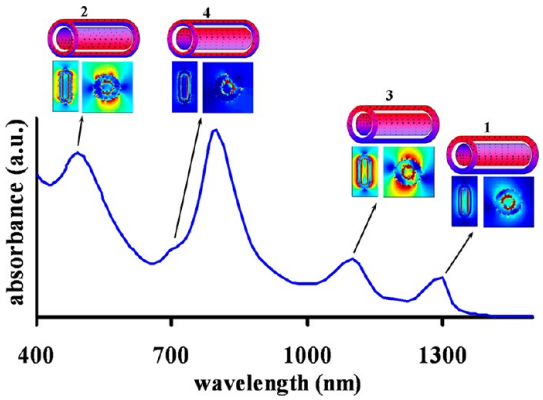

Figure 6. Theoretical analysis of the rod in shell with 3D finite-difference time-domain method. The calculated excitation spectra of the rod-in-shell with Drude–Lorentz model to fit bulk experimental dielectric constant of gold and silver from wavelength 450 to 1300 nm including both transverse and longitudinal polarization. The arrows represent the schematic of the rod-in-shell surface charge distribution and their corresponding transverse plasmon modes of cross section at short and long axis.

experiences two plasmons: (1) from the electron clouds of the shell, and (2) from the electron clouds of the core rod. In contrast to the shell, the cavity experiences the reverse phenomenon because it has a symmetric (w^+) repelling force to experience high energy and asymmetric (w^-) attraction with low energy. By considering this concept, we present our preliminary simulation results for all four possible coupling modes of the shell and cavity plasmons, with a fixed particle size (long axis, 66 nm; short axis, 26 nm; shell, 6 nm; gap, 2 nm) dispersed in water solvents with a refractive index of 1.33. The 3D finite-difference time-domain method was used to calculate the scattering, absorption, and extinction spectra of the rod-in-shell structure. The metal parts were modeled using the Drude–Lorentz model[39] to fit the bulk experimental dielectric constant of Au and Ag from a wavelength range of 450 to 1300 nm. The shell consisting of Ag and Au was modeled with the random distribution of each component with a 1:1 ratio. The grid resolution is 1 nm. The same conversion result was obtained with a 0.5 nm resolution. The transverse mode is excited with the electric field polarized along the short axis of the rod-in-shell. The longitudinal mode has an incident electric field polarized along the long axis. This results in the first mode having an symmetric shell and an asymmetric cavity (w_-^-); the second mode with an asymmetric shell and a symmetric cavity (w_+^+); the third mode having both symmetric core and shell (w_-^+); and finally, the fourth mode having both asymmetric shell and cavity (w_+^-).

In these four modes, the first (w_-^-) and second (w_+^+) interactions express lowest 1300 nm and highest 487 nm energy band, respectively (Figure 6). In the last two interactions, the shell and the cavity experienced an opposite energy expression, leading to ambiguity. To solve this ambiguity, we followed the charge distribution principle by Wu and co-workers,[40] and accordingly, in our simulation, the symmetric shell and cavity plasmon (w_-^+) is expected to cause a 1100 nm band and the asymmetric shell and cavity plasmon (w_+^-) to have a weak 700 nm band. The 800 nm peak is caused by the longitudinal mode. The simulation behaviors shown in Figure 6 are sharp compared to the broad experimental value, which must have been caused by the inhomogeneity in the particle shape experimentally. The as-prepared rod-in-shells exhibit more of a peanut-shaped structure rather than the ideal cylinder that was used in the theoretical calculation.

In our preliminary simulation, the SP model splitting caused by the transverse mode dominates the NIR resonance. The splitting is more intense in our sample compared to previous studies because of the cylindrical symmetry. In addition, we also experience a strong polarization of the rod compared to the sphere, which favors the splitting of all four modes of hybridization. To enhance our understanding of the extinction behavior, the absorption and scattering contributions were theoretically calculated. In our simulation with the rod-in-shell dispersed in water, absorption dominates scattering in the sum of extinction, as depicted in the spectral behavior derived from the transverse mode (Supporting Information, Figure S3). However, we experimentally determined the intensities of these two NIR bands (*i.e.*, 1100 and 1280 nm), enhanced with colloidal concentration (Supporting Information, Figure S4). The concentration-dependent multiple absorption and scattering for the long wavelength range could be a probable reason for the intensity enhancement.

***In Vitro* and *in Vivo* Toxicity Evaluation.** The appearance of absorption bands in the second NIR window has made the rod-in-shell a potential NIR hyperthermia agent for photoinduced therapeutic studies. We chose two rod-in-shells (2 nm gap *versus* 6.5 nm gap) with a distinct intensity in NIR absorbance to examine their

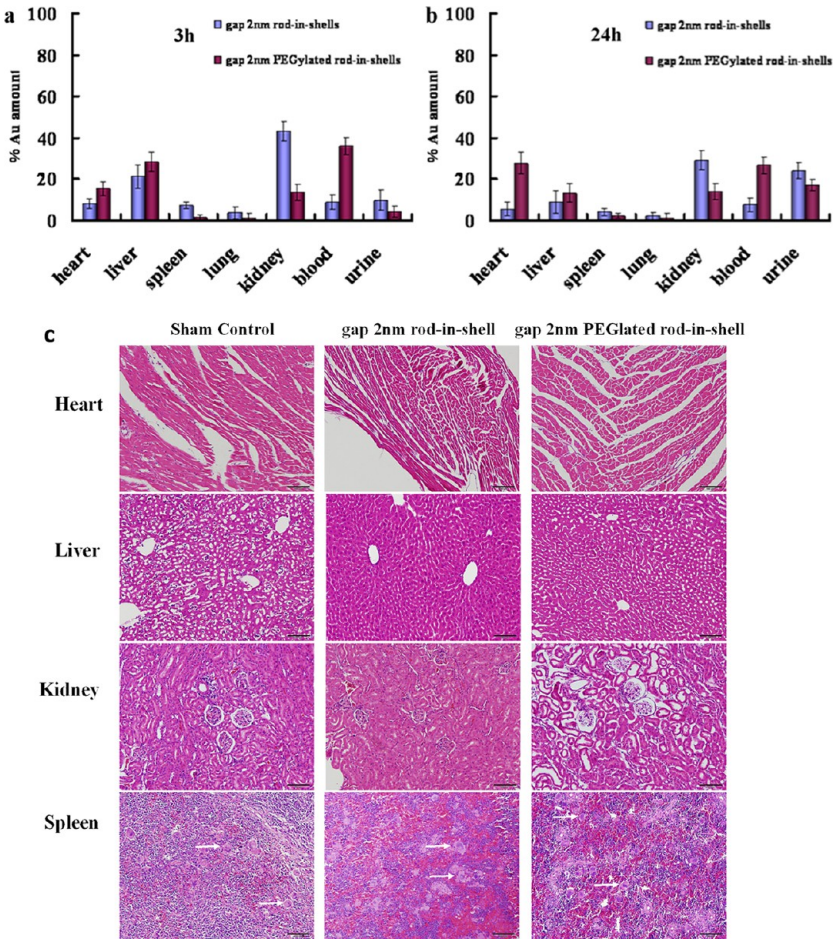

Figure 7. ICP analysis of biodistribution from Au rod-in-shells (gap 2 nm) and PEGylated Au rod-in-shells (gap 2 nm) after administration of 50 mg/kg to mice for (a) 3 h and (b) 24 h. (c) Hematoxylin and eosin stained histological images of four organ tissues (heart, liver, kidney, and spleen) from the mice treated with rod-in-shell and PEGylated rod-in-shell (gap 2 nm) particles after 24 h. The white arrows indicated in spleen are splenic follicles.

efficacy in NIR hyperthermia in the second NIR window. Both rod-in-shell structures were modified with bis-(amine) polyoxyethylene glycol (H_2N-PEG-NH_2, M_w, 6000). For PEGylated rod-in-shell preparation, 2-mercaptopropic acid (MPA) was used to form a Au−S bond on the surface of the rod-in-shell, changing the surface charge of the rod-in-shells from 3.3 to −33 mV. Subsequently, the amine groups of PEG formed amide bonds with the carboxylate groups of MPA through (1-ethyl-3-(3-dimethylaminopropyl) carbodiimide hydrochloride/*n*-hydroxysuccinimide (EDC/NHS). Quantification of the immobilized PEG was performed using a fluorescence-based method by reacting Rhodamine B isothiocyanate (RhBITC) with the exposed NH_2 group of PEG. The PEG conjugation amount was determined to be approximately 2432 molecules per rod-in-shell, which was derived from the difference in fluorescence intensity of RhBITC between the initial amount and the final residue in the supernatants, calculated based on a calibration curve according to the RhBITC concentration. A series of particle concentrations were incubated with LLC/LL2 lung cancer cells in 96-well plates for 24 h and then subjected to MTT measurements. The rod-in-shell alone (without PEGylated modification) showed a degree of toxicity at higher dosages. For example, the survival rate of cells drops to 80% when the dosage is up to 100 μg/mL (in the Au concentration), which is likely due to the Ag composition in the nanoshell causing toxicity (Supporting Information, Figure S5a,b). The FT-IR measurements show that cetyltrimethylammonium bromide (CTAB) was absent on the rod-in-shell surface. In contrast, PEGylated nanoparticles displayed no obvious toxic effect with a dosage of up to 200 ppm for the 2 and 6.5 nm gaps. Next, we evaluated the biodistribution by injecting the rod-in-shell and PEGylated rod-in-shell at 50 mg/kg into the tail vein of healthy mice (Figure 7). Because the 2 and 6.5 nm gaps have a similar particle size, we used the 2 nm gap to evaluate the biodistribution. All of the organs were surgically removed from the mice ($n = 3$; based on three mice) at 3 and 24 h after they were injected with the rod-in-shells. The rod-in-shell particles (without PEGylated modification) showed a dominant uptake in the kidneys and indicated an increase in metabolic excretion through urine at 24 h postinjection. The PEGylated rod-in-shell

particles (PEGylated modification) seem to preferentially appear in angiogenesis-related systems, where they show stable circulation in the blood and accumulation in the heart at 24 h postinjection. We resected and then dissected three organs (*i.e.*, the heart, liver, and kidney) for histological analysis at 24 h postinjection, all of which showed major particle accumulation. The removed tissues were stained with hematoxylin and eosin, and exhibited a well-organized cellular structure for the rod-in-shell particles (without PEGylation) and PEGylated rod-in-shells compared to the control samples (Figure 7c). Although *in vitro* studies using an MTT assay (Supporting Information, Figure S5a,b) have shown a degree of toxicity with a >100 ppm dose of rod-in-shell particles (without PEGylation), such toxicity was not observed in our histological analysis after 24 h. One possible factor could be associated with the quantity of rod-in-shell particles (without PEGylation) accumulated in the organs. We found that the number and size of splenic follicles increase in spleen-staining histological imaging from rod-in-shell particles (without PEGylation). The spleen is an efficient blood-filtering organ that plays the most important role in immune reactivity. Therefore, the morphological change of splenic follicles implicates that the rod-in-shell (without PEGylation) induces immune reactivity after 24 h. The PEGylated rod-in-shells show no appreciable abnormalities in the spleen.

***In Vitro* and *in Vivo* Photothermal Studies.** The MTT assay and histological analysis showed no acute toxicity for the PEGylated rod-in-shell particles. The NIR irradiation of the PEGylated rod-in-shell particles (2 and 6.5 nm gaps) was performed as a function of exposure time using a CW 1064 nm laser diode (a power density of 3 W/cm^2 and 2 W/cm^2, respectively) that overlaps with an SPR band of 1100 nm in the second NIR window. Two nanostructures were fixed at a concentration of 100 ppm. The NIR irradiation induces a temperature elevation in H_2O for both nanoparticle suspensions. A thermocouple was used to measure the bulk solution temperature. Both power densities displayed a faster temperature elevation for structures with the 2.0 nm gap (Figure 8). For example, particles with the 2 nm gap rapidly elevated the temperature to 50 °C at 6 min at 3 W/cm^2, whereas the temperatures of the structures with the 6.5 nm gap, with a considerably lower absorbance of approximately 1100 nm, increased slowly and reached only 29 °C under 6 min of irradiation. This demonstrates that the 2 nm gap can serve as a better photothermal mediator. When H_2O alone (in the absence of rod-in-shell particles) is exposed to 1064 nm irradiation, the water temperature is fixed at 25−26 °C, even with prolonged exposure. The photothermal killing of LLC/LL2 lung cancer cells was performed using 1064 nm at 3 W/cm^2 for 5 min of irradiation (Figure 9a). After NIR laser treatment, the cells were incubated with fluorescent labels of a calcein

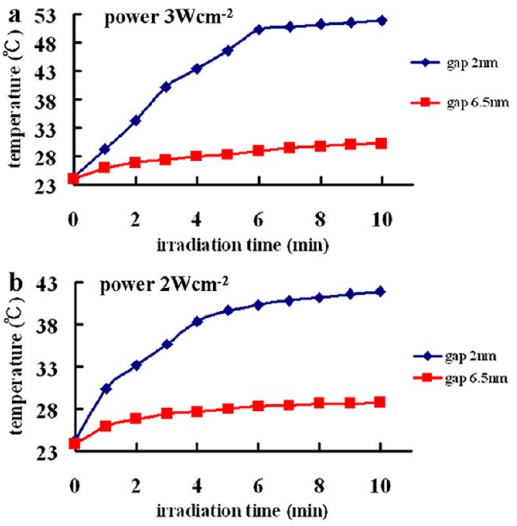

Figure 8. Temperature elevation profile under irradiation of 1064 nm CW diode laser for PEGylated rod-in-shell nanoparticles with gaps of 2 and 6.5 nm dispersed in H_2O; 100 ppm (in Au concentration) of rod-in-shell nanoparticles subject to (a) 3 W/cm^2 and (b) 2 W/cm^2 irradiation.

AM dye, producing green emission in viable cells, and we conducted observations under a fluorescence microscope. The control group of untreated cells showed no cell damage when exposed to NIR light. Cells treated with the 2 nm gap showed significant cell death in the area, lacking green fluorescence after 3 W/cm^2 of illumination. In contrast, cells treated with the 6.5 nm gap showed only slight cell damage by photodestruction. The temperature of the bulk solution was measured to be approximately 29 °C after NIR light irradiation for the 6.5 nm gap (Figure 8). The local temperature of the rod-in-shell with the 6.5 nm gap was expected to be higher than the measured bulk solution temperature (29 °C) after laser irradiation, thereby resulting in a degree of cell destruction, as observed in Figure 9a. The white dashed circles indicate the laser beam area. We found that the area of cells damaged by the 2 nm gap is larger than the laser beam spot, indicating efficient hyperthermia derived from the rod-in-shell structure. The same phenomenon was observed when the cancer cells treated with the 2 nm gap were subjected to irradiation by using an 808 nm diode laser (*vide infra*). The rod-in-shell particles were stable after 1064 nm laser irradiation. No structure destruction was observed in the TEM images recorded after 20 min of laser exposure.

We extended the studies from *in vitro* to *in vivo* to investigate the regression efficacy in tumor growth with the two rod-in-shell structures (*i.e.*, 2 and 6.5 nm gaps) by using a 1064 nm diode laser. The xenografted mouse tumor model was established using the subdermal injection of LLC/LL2 lung cancer cells. Fifteen B6 mice bearing LLC/LL2 tumors were divided into the following three groups: (1) laser only; (2) the 6.5 nm gap + the laser; and (3) the 2 nm gap + the laser. Afterward,

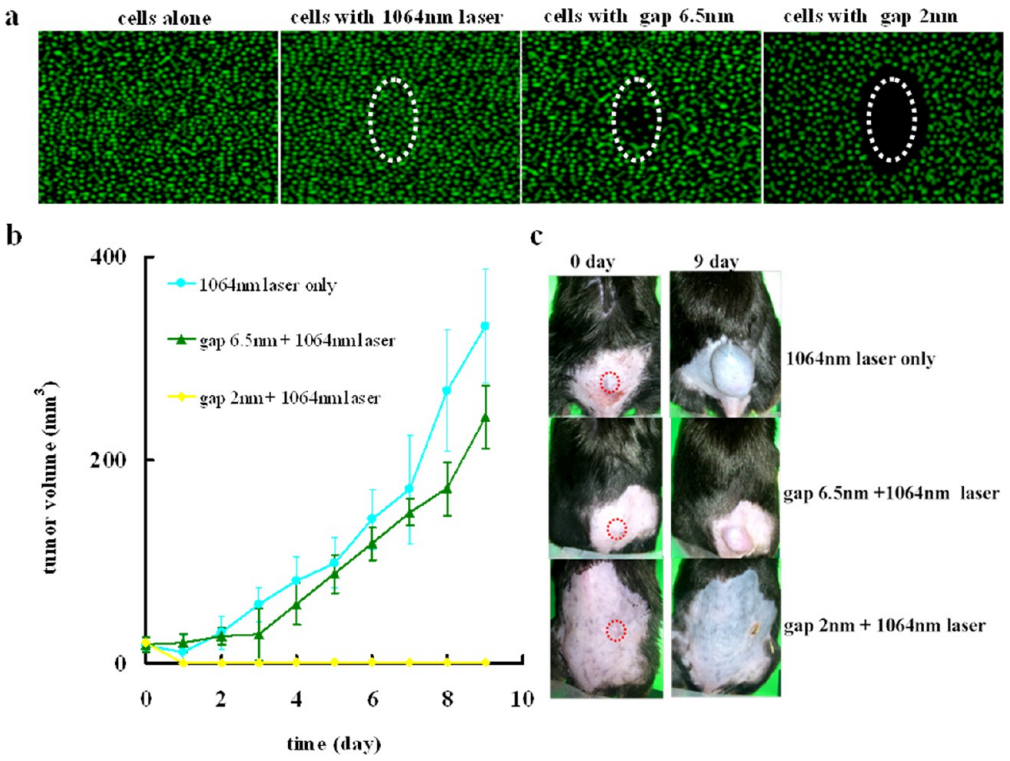

Figure 9. (a) LLC/LL2 lung cancer cells treated with gap 6.5 nm and gap 2 nm rod-in-shells were irradiated using a diode 1064 nm laser at 3 W cm^{-2} for 5 min of exposure. The group of "cells with laser" was performed without treatment of rod-in-shell and exposed to laser. The white dotted circles indicate the laser beam area. The green fluorescence of calcein-AM indicate living cells. (b) Time-dependent tumor growth as a function of postirradiation days. The tumors were exposed to a diode laser with a wavelength of 1064 nm using a laser power density of 3 W/cm^2 for 7 min. (c) Photographs of the mice taken before (0 day) and at day 9 after NIR laser irradiation. The red dotted circles indicate the location of the tumors.

all tumors were measured over time. For the laser ablation of solid tumors, the mice bearing tumors (approximately 20 mm^3) were locally injected with the rod-in-shell particles at 50 mg/kg and subjected to a 1064 nm diode laser for 7 min of irradiation (3 W/cm^2) (Figure 9b). The mice injected with the 2 nm gap showed effective suppression of tumor growth with one-time irradiation. External observation showed that the tumors had disappeared completely in four mice by Day 2, and they continued to show no sign of tumor regrowth by Day 9. By 9 days after one-time laser ablation, the 2 nm gap-injected mice exhibited only black scars on the skin at the tumor location (Figure 9c). The tumor of the remaining fifth mouse showed evidence of recurrence at Day 6 because of the regrowth of surviving cancer cells. The tumor growth was completely suppressed after we treated the regrown tumor with one more shot of laser irradiation for the fifth mouse. Conversely, laser irradiation alone and the irradiated mice treated with the 6.5 nm gap had tumors that continued to grow over time. The 6.5 nm gap displays poor efficacy in regressing tumor growth in photothermal ablation performance, which is consistent with *in vitro* cell studies.

In addition to serving as a hyperthermia agent in the second NIR window, the rod-in-shell structures have strong absorbance at 800 nm of the first NIR window as well. Therefore, a comparison with Au NRs and an evaluation of the laser ablation efficacy (2 nm gap) of solid tumors by using a CW diode laser of 808 nm was deemed necessary The comparison can be conducted because the UV−vis absorption spectrum of Au NRs is observable with the spectra of the rod-in-shells, measured under the same Au concentration (Figure 5). Following this approach, the Au NRs were modified with MPA and PEG before use. The FT-IR spectra indicated the disappearance of a CTAB surfactant on the surface of the Au NRs (Supporting Information, Figure S6) after PEGylated modification. The MTT assays also supported the successful conjugation of PEG on Au NRs (Supporting Information, Figure S5c). No toxicity was observed from the PEGylated Au NRs, whereas the cell viability dropped to 60% with a 200 ppm dosage for the CTAB-coated Au NR because of the presence of a CTAB surfactant on the surface. Prior to *in vitro* and *in vivo* hyperthermia evaluation, the solution temperature after laser irradiation was raised using an 808 nm diode laser, and the results showed that both the 2 nm gap and the Au NR can readily raise temperature with longer exposure (Figure 10). However, the 2 nm gap led to a higher temperature compared to Au NRs under the same irradiation period at a fixed laser intensity. *In vitro* photothermal ablation of the LLC/LL2 lung cancer cells was conducted at

3 W/cm^2 for 5 min of irradiation (Figure 11a). The cells treated without a nanomaterial did not experience destruction when exposed to laser, and the same result was obtained using the 1064 nm laser. The targeted cells treated with the PEGylated Au NRs or PEGylated rod-in-shells (2 nm gap) irradiated using the 808 nm

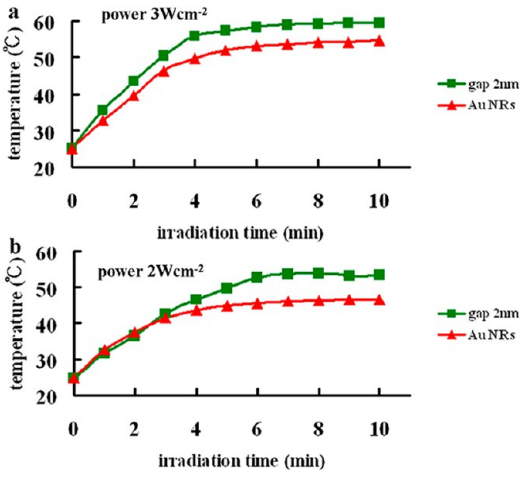

Figure 10. Temperature elevation profile under irradiation of 808 nm CW diode laser for PEGylated rod-in-shell nanoparticles with gap 2 nm and PEGylated Au nanorods dispersed in H_2O; 100 ppm (in Au concentration) of nanoparticles subject to (a) 3 W/cm^2 and (b) 2 W/cm^2 irradiation.

CW diode laser caused apparent cell damage at 3 W/cm^2 of illumination. As shown with the use of the 1064 nm diode laser, the PEGylated rod-in-shells (2 nm gap) yielded a larger destruction area beyond the laser beam spot, whereas the area damaged by the Au NRs was limited to the irradiation area. Although we cannot provide a reasonable interpretation regarding the rod-in-shells having caused damage beyond the laser beam at this stage, it may possibly be due to the incorporation of Ag in the rod-in-shell nanostructure. Silver has a greater thermal conductivity than gold; the thermal conductivity for bulk Ag (429 $Wm^{1-}K^{-1}$) is larger than that for bulk Au (318 $Wm^{1-}K^{-1}$).[41] After NIR laser irradiation, the heat generated by the rod-in-shell deposited readily between particles adjacent to the irradiated area, thereby resulting in damage outside the irradiated spot. The other possibility might be due to the rod-in-shells (2 nm gap) being good optothermal converters. Because of the diffraction of the laser property, the actual beam is larger than the area of the dotted circle when observed by the naked eye. Thus, the laser energy outside the dotted circles would still be heated effectively to kill cancer cells. Based on the TEM image, the rod-in-shell particles again showed no structural destruction after 20 min of exposure to the 808 nm diode laser. In contrast, Au NRs essentially retain their structure after 7 min of laser irradiation, but

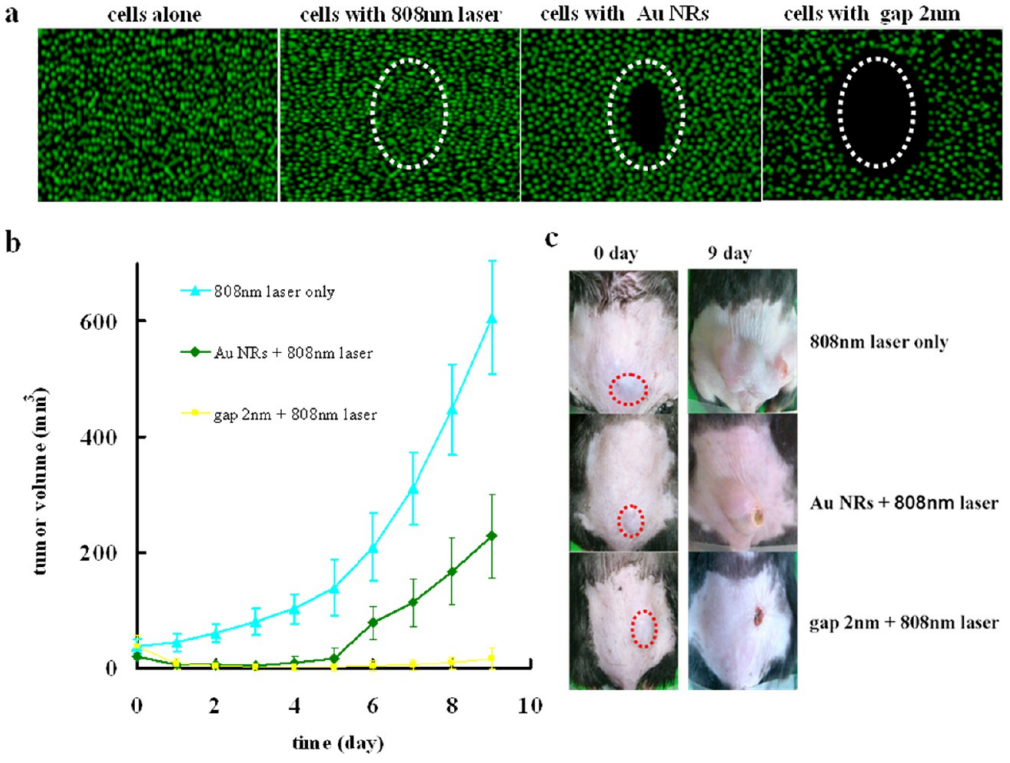

Figure 11. (a) LLC/LL2 lung cancer cells treated with Au NRs and gap 2 nm rod-in-shells were irradiated using a diode 808 nm laser at 3 Wcm^{-2} for 5 min of exposure. The group of "cells with laser" was performed without treatment of rod-in-shell and exposed to laser. The white dotted circles indicate the laser beam area. The green fluorescence of calcein-AM indicate living cells. (b) Time-dependent tumor growth as a function of postirradiation days. The tumors were exposed to a diode laser with a wavelength of 808 nm using a laser power density of 3 W/cm^2 for 7 min. (c) Photographs of the mice taken before (0 day) and at day 9 after NIR laser irradiation. The red dotted circles indicate the location of the tumors.

start exhibiting partial morphological damage from the longitudinal poles after 10 min of exposure. The drastic change in shape appears after 20 min of irradiation (Supporting Information, Figure S7).

We further evaluated photothermal cancer therapy in the *in vivo* animal model by measuring the tumor growth for PEGylated Au NRs and PEGylated rod-in-shells (2 nm gap). Using the same approach that was applied for the 1064 nm laser, 15 mice bearing LLC/LL2 tumors (approximately 20 mm^3) were divided between three cohorts (*i.e.*, laser only, PEGylated Au NRs + laser, PEGylated rod-in-shells (2 nm gap) + laser). The particles (50 mg/kg) were intratumorally injected into the tumor site, and then subjected to laser illumination for 7 min at 3 W/cm^2. The rod-in-shell (2 nm gap) was shown to have a highly efficient therapeutic effect on the laser ablation of solid tumors (Figure 11b). One-time laser irradiation caused complete regression in two mice by Day 2, whereas the tumor in the fifth mouse relapsed at Day 6 after initial growth inhibition. The PEGylated Au NRs injected in five mice were shown to suppress tumor growth on Day 2, but without complete regression. We subsequently observed that the tumor sizes remained unchanged until Day 5, when recurrence occurred. The laser irradiation alone group showed no sign of tumor inhibition, with the tumors continuing to grow over 9 days of observation. In our comparison, the rod-in-shell particles show greater anticancer efficacy compared to Au NRs *in vitro* and *in vivo*.

CONCLUSION

We present the first demonstration for the *in vitro* and *in vivo* photothermal killing of cancer cells in the second NIR window. The fabrication of Au NRs smaller than 100 nm and their subsequent conversion to a rattle-like (rod-in-shell) structure have enabled us to perform hyperthermia-based therapy in the first and second NIR windows. The UV−vis−NIR spectrum behavior of the rod-in-shell is sensitive to the gap distance between the Au NR (core) and the nanoshell. The *in vitro* performance clearly showed high efficacy in the NIR photothermal destruction of cancer cells, where we observed that large cells experienced damage beyond the laser-irradiated area. We believe that such a marked phenomenon has made the rod-in-shell a practical and powerful hyperthermia agent. The photothermal ablation of solid tumors demonstrates that the rod-in-shell is more efficacious compared to Au NRs when NIR hyperthermia was conducted using an 808 nm diode laser.

MATERIALS AND METHODS

Materials. All working solutions were prepared using doubly distilled water. Chemicals used were of analytical grade hydrogen tetrachloroaurate (III) hydrate ($HAuCl_4 \cdot 3H_2O$, Alfa Aeser, 99.99%), cetyltrimethylammonium bromide (CTAB, Fluka, 96%), ascorbic acid (AA, Riedel-deHaen, M_w, 176.13; 99.7%), silver nitrate ($AgNO_3$, Sigma-Aldrich, M_w, 169.87; 99.8%), sodium borohydride ($NaBH_4$, Sigma-Aldrich, M_w, 37.83; 99%), polyvinylpyrrolidone (PVP, Sigma-Aldrich, M_w, 130000), 3-mercaptopropionic acid (MPA, Fluka, M_w, 106.14; 99%), toluidine blue O (TBO, Acros Organics, M_w, 305.82), bis(amine) polyoxyethylene glycol (PEG, Sigma-Aldrich, M_w, 6000), *N*-(3-dimethylaminopropyl)-*N*′-ethylcarbodiimide hydrochloride (EDC, Sigma-Aldrich, M_w, 155.24), *N*-hydroxysulfosuccinimide sodium salt (NHS, Sigma-Aldrich, M_w, 217.13; ≥98.5%).

Instrumentation. Low magnification transmission electron microscopy (TEM) images were recorded using a Hitachi H-7500 electron microscope, and high resolution transmission electron microscopy (HRTEM) images were recorded using a JEOL JEM-2100F electron microscope. Inductively coupled plasma (ICP) analysis for elemental composition was analyzed using a Jobin Yvon JY138 spectroanalyzer. For the ICP analysis, nanostructures were digested in aqua regia. Absorption spectra of all the nanostructures were recorded in the UV−vis−NIR region using UV−vis−NIR spectrophotometer (JASCO, V-670). Surface charge density measured by the Zeta sizer Nano-zs90. Fluorescence spectra were measured using HORIBA Fluoromax-4 spectrometer. Nitrogen (N2) adsorption measurements were taken at 77 K using an accelerated surface area and porosimetry analyzer (ASAP 2010; Micrometrics Instrument Corporation, Norcross, GA) with Brunauer−Emmett−Teller (BET) calculations for the surface area.

Preparation of Au Nanorods (Au NRs). A 100 mL aliquot of a 0.5 mM $HAuCl_4$ precursor solution (prepared by mixing 5 mL of 5 mM $HAuCl_4$ with 5 mmol CTAB, and raising the volume to 50 mL with H_2O) was vigorously stirred, and 120 μL of a 100 mM $AgNO_3$ solution was added dropwise. After 5 min, 600 μL of a 100 mM ascorbic acid (AA) solution was added, followed by 40 μL of a 1.6 mM $NaBH_4$ solution, and the mixture was stirred for 150 min. The obtained suspension was centrifuged at 13 000 rpm for 12 min. The supernatant was discarded, and the precipitate was repeatedly washed with H_2O under sonication, followed by centrifugation under the same conditions. Finally, the Au NRs were dispersed in H_2O for subsequent Au NR@Ag synthesis.

Preparation of the Au NR@Ag. In brief, the Au NRs were redispersed in a 50 mM CTAB solution to obtain 1 mL of the NR solution with a Au concentration of 50 ppm. This solution was then added to 5 mL of a 1 wt % PVP solution, followed by sequentially adding different $AgNO_3$ concentrations (*i.e.*, C_{AgNO_3} = 1 mM for a 7−8 nm Ag shell to generate 2 and 4 nm gaps or 1.23 mM for a 9−10 nm Ag shell to generate the 6.5 nm gap), 0.125 mL of 100 mM AA, and 0.25 mL of 0.1 M NaOH solutions. The mixture was stirred slowly for 10 min. The obtained orange-red solution is called Au NR@Ag core−shell-type NRs. The resulting Au NR@Ag colloids were centrifuged at 10 000 rpm for 10 min, and the supernatant was discarded before the precipitate was washed with H_2O under sonication, followed by centrifugation under the same conditions, and finally, redispersion in H_2O.

Preparation of Au Rod-in-Shells. To prepare the Au rod-in-shell, a Ag nanoshell in the Au NR@Ag obtained from the procedure after washing was replaced with Au by slowly adding different volumes of 1 mM $HAuCl_4$ aqueous solutions (V_{HAuCl_4} = 700 μL for the 2.0 nm gap, 550 μL for the 4.0 nm gap, and 400 μL for the 6.5 nm gap) to the Au NR@Ag prepared from 1 mM, 1 mM, and 1.23 mM $AgNO_3$, respectively. In total, 550 μL of a 0.94 mM Au NR@Ag (based on Ag ion concentration) was dispersed in 5.75 mL H_2O, followed by the sequential addition of 500 μL of 100 mM CTAB and 125 μL of 100 mM AA. This mixture was placed under a vigorous stirring condition, and different volumes of $HAuCl_4$ were added, as mentioned. After 16 min, the reaction was stopped, and the products were purified by washing with a saturated NaCl solution, followed by repeated H_2O washing by centrifugation at 10 000 rpm for 10 min, and then redispersion in H_2O for further characterization.

PEG Conjugation of the Rod-in-Shells. The rod-in-shell with a concentration of 50 μg/mL was dispersed in a PBS buffer solution, which was mixed with 50 μL of 10 mM EDC and 50 μL of 10 mM NHS before sonication for 30 min at room temperature. After the addition of 100 μL PEG (10 mM), the reaction was allowed to continue under sonication at room temperature for another 6 h. The resultant solution was centrifuged at 10 000 rpm for 10 min at room temperature, and the supernatants were removed. The remaining precipitates were repeatedly washed with H_2O by centrifugation, as mentioned. To assess the amount of PEG bound to the Au NR-in-shell surface, the fluorescence tag (i.e., the rhodamine B isothiocyanate (RhBITC) molecule with the N═C═S group conjugate on the amine group of PEG) was used. After 20 μL of 1 mM RhBITC was added to these PEGylated rod-in-shell conjugates at room temperature, they were reacted for 6 h. The RhBITC-conjugated PEGylated rod-in-shells were collected following a centrifugation−wash process. The supernatants were then subjected to fluorescence detection. The luminescence emission of RhBITC at 552 nm was measured to identify the concentration of RhBITC bound to the PEGylated rod-in-shell with the corresponding calibration curve.

Temperature Elevation Profile by Photothermal Conversion. We added 200 μL of 100 ppm (in Au concentration) of the rod-in-shell (with the 2.0 or 6.5 nm gap) or the Au NRs in 96-well plates. The efficiency of the increase in the photoinduced temperature of the solution was investigated under various irradiation times by using a CW NIR laser. The change in solution temperature was determined using a digital thermometer (TES 1319A-K type).

Cell Culture. The LLC/LL2 lung cancer cells were cultured in Dulbecco's modified Eagle's medium (DMEM, Cellgro) with 10% fetal bovine serum (FBS, Gem Cell) at 37 °C under 5% CO_2. The cells were collected by trypsinization, placed onto a 10 cm tissue culture Petri-dish, and allowed to grow for 3 days.

Cytotoxicity Assay (MTT). The cells were seeded at a density of 5×10^3 per well in a 96-well culture plate and were incubated overnight at 37 °C with 5% CO_2. For the no laser exposure condition, a different concentration of the rod-in-shell was added to the medium and incubated for 24 h in the dark to examine the cytotoxicity. To perform MTT, the culture medium with the nanomaterial was removed and replaced with the new culture medium containing MTT reagents (10%) (Sigma) followed by incubation for 4 h at 37 °C, allowing the formation of formazan crystals. The crystals were dissolved in DMSO (200 μL) and incubated in the dark for another 10 min, followed by centrifugation at 4000 rpm for 10 min. The supernatant was transferred onto a new ELISA plate, and the absorbance was measured at a wavelength of 540 nm by using an ELISA reader.

Tumor-Bearing Animal Model. The LLC/LL2 lung cancer cells were maintained in DMEM (GIBCO, Taiwan). The medium was supplemented with 10% fetal bovine serum (FBS; GIBCO, Taiwan) and penicillin-streptomycin (100 μg/mL). The cell line was incubated at 37 °C with 5% CO_2 in air. The cells were trypsinized from the tissue culture flasks and washed twice with PBS, and were then counted on a hemacytometer slide and resuspended in serum-free, antibiotic-free normal saline before injection. The male B6 mice (6 weeks old) were provided by the National Cheng Kung University (NCKU) Laboratory Animal Center (Tainan, Taiwan). All animals received humane care in compliance with NCKU guidelines for the maintenance and use of laboratory animals in research. All of the experimental protocols involving live animals were reviewed and approved by the Animal Experimentation Committee of NCKU. The LLC/LL2 tumor xenografts were established through a subcutaneous dorsal flank injection of 10^6 tumor cells in 100 μL of normal saline by using a 27G needle. A visible tumor, usually observed 1 week after implantation, received laser illumination. The tumor size was measured along the longest width and the corresponding perpendicular length. The tumor volume was calculated using the volume of an ellipsoid, where volume = $4\pi/3$ (length/2 $\times$ width/2 $\times$ depth/2). This study assumed that depth = width and $\pi = 3$, resulting in volume = $^1/_2 \times$ length $\times$ (width)^2. Prior to laser exposure, the animals were anesthetized using 2% isoflurane (Abbott Laboratories, Abbott Park, IL) mixed with 100% O_2 and delivered using a veterinary anesthesia delivery system (ADS 1000; Engler Engineering Corp., Hialeah, FL).

Conflict of Interest: The authors declare no competing financial interest.

Acknowledgment. This work was supported by the National Science Council (NSC101-2113-M-006-004-MY2) of Taiwan.

Supporting Information Available: N_2 adsorption−desorption profile, TEM, UV−vis, FTIR spectra, and the MTT assay of the as-obtained Au rod-in-shells and Au NRs. This material is available free of charge *via* the Internet at http://pubs.acs.org.

REFERENCES AND NOTES

1. Smith, A. M.; Mancini, M. C.; Nie, S. Bioimaging: Second Window for *in Vivo* Imaging. *Nat. Nanotechnol.* **2009**, *4*, 710–711.
2. Welsher, K.; Sherlock, S. P.; Dai, H. Deep-Tissue Anatomical Imaging of Mice Using Carbon Nanotube Fluorophores in the Second Near-Infrared Window. *Proc. Natl. Acad. Sci. U. S.A.* **2011**, *108*, 8943–8948.
3. Hong, G.; Robinson, J. T.; Zhang, Y.; Diao, S.; Antaris, A. L.; Wang, Q.; Dai, H. *In Vivo* Fluorescence Imaging with Ag_2S Quantum Dots in the Second Near-Infrared Region. *Angew Chem. Int. Ed.* **2012**, *51*, 9818–9821.
4. Shi, S.; Zhu, X.; Zhao, Z.; Fang, W.; Chen, M.; Huang, Y.; Chen, X. Photothermally Enhanced Photodynamic Therapy Based on Mesoporous Pd@Ag@*m*SiO_2 Nanocarriers. *J. Mater. Chem. B* **2013**, *1*, 1133–1141.
5. Chu, M.; Peng, J.; Zhao, J.; Liang, S.; Shao, Y.; Wu, Q. Laser Light Triggered-Activated Carbon Nanosystem for Cancer Therapy. *Biomaterials* **2013**, *34*, 1820–1832.
6. Liu, H.; Liu, T.; Wu, X.; Li, L.; Tan, L.; Chen, D.; Tang, F. Targeting Gold Nanoshells on Silica Nanorattles: A Drug Cocktail to Fight Breast Tumors *via* a Single Irradiation with Near-Infrared Laser Light. *Adv. Mater.* **2012**, *24*, 755–761.
7. Cheng, L.; Yang, K.; Chen, Q.; Liu, Z. Organic Stealth Nanoparticles for Highly Effective *in Vivo* Near-Infrared Photothermal Therapy of Cancer. *ACS Nano* **2012**, *6*, 5605–5613.
8. Chu, M.; Pan, X.; Zhang, D.; Wu, Q.; Peng, J.; Hai, W. The Therapeutic Efficacy of CdTe and CdSe Quantum Dots for Photothermal Cancer Therapy. *Biomaterials* **2012**, *33*, 7071–7083.
9. Zhou, F.; Wu, S.; Song, S.; Chen, W. R.; Resasco, D. E.; Xing, D. Antitumor Immunologically Modified Carbon Nanotubes for Photothermal Therapy. *Biomaterials* **2012**, *33*, 3235–3242.
10. Melancon, M. P.; Zhou, M.; Li, C. Cancer Theranostics with Near-Infrared Light-Activatable Multimodal Nanoparticles. *Acc. Chem. Res.* **2011**, *44*, 947–956.
11. Liu, H.; Chen, D.; Li, L.; Liu, T.; Tan, L.; Wu, X.; Tang, F. Multifunctional Gold Nanoshells on Silica Nanorattles: A Platform for the Combination of Photothermal Therapy and Chemotherapy with Low Systemic Toxicity. *Angew. Chem., Int. Ed.* **2011**, *50*, 891–895.
12. Lee, S. M.; Park, H.; Yoo, K. H. Synergistic Cancer Therapeutic Effects of Locally Delivered Drug and Heat Using Multifunctional Nanoparticles. *Adv. Mater.* **2010**, *22*, 4049–4053.
13. Gobin, A.; Lee, M.; Halas, N.; James, W.; Drezek, R.; West, J. Near-Infrared Resonant Nanoshells for Combined Optical Imaging and Photothermal Cancer Therapy. *Nano Lett.* **2007**, *7*, 1929–1934.
14. Hirsch, L.; Stafford, R.; Bankson, J.; Sershen, S.; Rivera, B.; Price, R.; Hazle, J.; Halas, N.; West, J. Nanoshell-Mediated Near-Infrared Thermal Therapy of Tumors Under Magnetic Resonance Guidance. *Proc. Natl. Acad. Sci. U.S.A.* **2003**, *100*, 13549–13554.
15. Bakueva, L.; Gorelikov, I.; Musikhin, S.; Zhao, X. S.; Sargent, E. H.; Kumacheva, E. PbS Quantum Dots with Stable Efficient Luminescence in the Near-IR Spectral Range. *Adv. Mater.* **2004**, *16*, 926–929.
16. Semonin, E.; Johnson, J. C.; Luther, J. M.; Midgett, A. G.; Nozik, A. J.; Beard, M. C. Absolute Photoluminescence

Quantum Yields of IR-26 Dye, PbS, and PbSe Quantum Dots. *J. Phys. Chem. Lett.* **2010**, *1*, 2445–2450.
17. Huang, X.; Tang, S.; Mu, X.; Dai, Y.; Chen, G.; Zhou, Z.; Ruan, F.; Yang, Z.; Zhang, N. Freestanding Palladium Nanosheets with Plasmonic and Catalytic Properties. *Nat. Nanotechnol.* **2011**, *6*, 28–32.
18. Huang, X.; Tang, S.; Liu, B.; Ren, B.; Zheng, N. Enhancing the Photothermal Stability of Plasmonic Metal Nanoplates by a Core–Shell Architecture. *Adv. Mater.* **2011**, *23*, 3420–3425.
19. Zhang, Z.; Wang, L.; Wang, J.; Jiang, X.; Li, X.; Hu, Z.; Ji, Y.; Wu, X.; Chen, C. Mesoporous Silica-Coated Gold Nanorods as a Light-Mediated Multifunctional Theranostic Platform for Cancer Treatment. *Adv. Mater.* **2012**, *24*, 1418–1423.
20. Gormley, A. J.; Larson, N.; Sadekar, S.; Robinson, R.; Ray, A.; Ghandehari, H. Guided Delivery of Polymer Therapeutics Using Plasmonic Photothermal Therapy. *Nano Today* **2012**, *7*, 158–167.
21. Choi, W.; Kim, J. Y.; Kang, C.; Byeon, C. C.; Kim, Y. H.; Tae, G. Tumor Regression *in Vivo* by Photothermal Therapy Based on Gold-Nanorod-Loaded, Functional Nanocarriers. *ACS Nano* **2011**, *5*, 1995–2003.
22. Jang, B.; Park, J. Y.; Tung, C. H.; Kim, I. H.; Choi, Y. Gold Nanorod–Photosensitizer Complex for Near-Infrared Fluorescence Imaging and Photodynamic/Photothermal Therapy *in Vivo*. *ACS Nano* **2011**, *5*, 1086–1094.
23. Park, J. H.; Maltzahn, G. V.; Ong, L. L.; Centrone, A.; Hatton, T. A.; Ruoslahti, E.; Bhatia, S. N.; Sailor, M. J. Cooperative Nanoparticles for Tumor Detection and Photothermally Triggered Drug Delivery. *Adv. Mater.* **2010**, *22*, 880–885.
24. Shiotani, A.; Akiyama, Y.; Kawano, T.; Niidome, Y.; Mori, T.; Katayama, Y.; Niidome, T. Active Accumulation of Gold Nanorods in Tumor in Response to Near-Infrared Laser Irradiation. *Bioconjugate Chem.* **2010**, *21*, 2049–2054.
25. Maltzahn, G. V.; Park, J. H.; Agrawal, A.; Bandaru, N. K.; Das, S. K.; Sailor, M. J.; Bhatia, S. N. Computationally Guided Photothermal Tumor Therapy Using Long-Circulating Gold Nanorod Antennas. *Cancer Res.* **2009**, *69*, 3892–3900.
26. Huff, T.; Tong, L.; Zhao, Y.; Hansen, M.; Cheng, J.; Wei, A. Hyperthermic Effects of Gold Nanorods on Tumor Cells. *Nanomedicine* **2007**, *2*, 125–132.
27. Hunag, X.; El-Sayed, I.; Qian, W.; El-Sayed, M. Cancer Cell Imaging and Photothermal Therapy in the Near-Infrared Region by Using Gold Nanorods. *J. Am. Chem. Soc.* **2006**, *128*, 2115–2120.
28. Perez-Juste, J.; Liz-Marzan, L. M.; Carnie, S.; Chan, D. Y. C.; Mulvaney, P. Electric-Field-Directed Growth of Gold Nanorods in Aqueous Surfactant Solutions. *Adv. Funct. Mater.* **2004**, *14*, 571–579.
29. Payne, E. K.; Shuford, K. L.; Park, S.; Schatz, G. C.; Mirkin, C. A. Multipole Plasmon Resonances in Gold Nanorods. *J. Phys. Chem. B* **2006**, *110*, 2150–2154.
30. Perez-Juste, J.; Pastoriza-Santos, I.; Liz-Marzan, L. M.; Mulvaney, P. Gold Nanorods: Synthesis, Characterization and Applications. *Coord. Chem. Rev.* **2005**, *249*, 1870–1901.
31. Kang, S. K.; Kim, Y.; Hahn, M. S.; Choi, I.; Lee, J.; Yi, J. Aspect Ratio Control of Au Nanorods *via* Temperature and Hydroxylamine Concentration of Reaction Medium. *Curr. Appl. Phys.* **2006**, *651*, e114–e120.
32. Wijaya, A.; Schaffer, S. B.; Pallares, I. G.; Hamad-Schifferli, K. Selective Release of Multiple DNA Oligonucleotides from Gold Nanorods. *ACS Nano* **2009**, *3*, 80–86.
33. Jana, N.; L.Gearheart, R.; Murphy, C. J. Wet Chemical Synthesis of High Aspect Ratio Cylindrical Gold Nanorods. *J. Phys. Chem. B* **2001**, *105*, 4065–4067.
34. Liu, M.; Guyot-Sionnest, P. Synthesis and Optical Characterization of Au/Ag Core/Shell Nanorods. *J. Phys. Chem. B* **2004**, *108*, 5882–5888.
35. Park, K.; Drummy, L. F.; A Vaia, R. Ag Shell Morphology on Au Nanorod Core: Role of Ag Precursor Complex. *J. Mater. Chem.* **2011**, *21*, 15608–15618.
36. Xiang, Y.; Wu, X.; Liu, D.; Li, Z.; Chu, W.; Feng, L.; Zhang, K.; Zhou, W.; Xie, S. Gold Nanorod-Seeded Growth of Silver Nanostructures: From Homogeneous Coating to Anisotropic Coating. *Langmuir* **2008**, *24*, 3465–3470.
37. Prodan, E.; Radloff, C.; Halas, N. J.; Nordlander, P. A. A Hybridization Model for the Plasmon Response of Complex Nanostructures. *Science* **2003**, *302*, 419–422.
38. Bardhan, R.; Mukherjee, S.; Mirin, N. A.; Levit, S. D.; Nordlander, P.; Halas, N. J. Nanosphere-in-a-Nanoshell: A Simple Nanomatryushka. *J. Phys. Chem. C* **2010**, *114*, 7378–7383.
39. *Advances in FDTD Computation Electrodynamics: Photonics and Nanotechnology*; Taflove, A., Ed.; Artech House: Boston, MA, 2013.
40. Jian, Z.; Jun, L. J.; Wu, Z. J. Tuning the Dipolar Plasmon Hybridization of Multishell Metal–Dielectric Nanostructure: Gold Nanosphere in a Gold Nanoshell. *Plasmonics* **2011**, *6*, 527–534.
41. *Chemical Rubber Company Handbook of Chemistry and Physics*, 79th ed.; Lide, D. R., Ed.; CRC Press: Boca Raton, FL, 1998.